Article

Multifunctional P-Doped TiO₂ Films: A New Approach to Self-Cleaning, Transparent Conducting Oxide Materials

Carlos Sotelo-Vazquez,[†] Nuruzzaman Noor,[†] Andreas Kafizas,[†,‡] Raul Quesada-Cabrera,[†] David O. Scanlon,[§,∥] Alaric Taylor,[⊥] James R. Durrant,[‡] and Ivan P. Parkin*[,†]

[†]Materials Chemistry Research Centre, Department of Chemistry, University College London, 20 Gordon Street, London WC1H 0AJ, United Kingdom

[‡]Department of Chemistry, Imperial College London, Exhibition Road, London SW7 2AZ, United Kingdom

[§]Kathleen Lonsdale Materials Chemistry, Department of Chemistry, University College London, 20 Gordon Street, London WC1H 0AJ, United Kingdom

[∥]Diamond House, Harwell Science and Innovation Campus, Diamond Light Source Ltd., Didcot, Oxfordshire OX11 0DE, United Kingdom

[⊥]Department of Electronic & Electrical Engineering, University College London, Torrington Place, London WC1E 7JE, United Kingdom

S *Supporting Information*

ABSTRACT: Multifunctional P-doped TiO₂ thin films were synthesized by atmospheric pressure chemical vapor deposition (APCVD). This is the first example of P-doped TiO₂ films with both P^{5+} and P^{3-} states, with the relative proportion being determined by synthesis conditions. This technique to control the oxidation state of the impurities presents a new approach to achieve films with both self-cleaning and TCO properties. The origin of electrical conductivity in these materials was correlated to the incorporation of P^{5+} species, as suggested by Hall Effect probe measurements. The photocatalytic performance of the films was investigated using the model organic pollutant, stearic acid, with films containing predominately P^{3-} states found to be vastly inferior photocatalysts compared to undoped TiO₂ films. Transient absorption spectroscopy studies also showed that charge carrier concentrations increased by several orders of magnitude in films containing P^{5+} species only, whereas photogenerated carrier lifetimes—and thus photocatalytic activity—were severely reduced upon incorporation of P^{3-} species. The results presented here provide important insights on the influence of dopant nature and location within a semiconductor structure. These new P-doped TiO₂ films are a breakthrough in the development of multifunctional advanced materials with tuned properties for a wide range of applications.
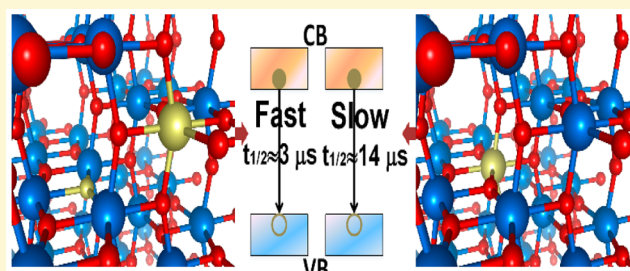
1. INTRODUCTION

Titania (TiO₂) is the most widely studied photocatalytic material as it is highly active, durable to extended photocatalytic cycling, mechanically robust, and largely chemically inert over a wide range of pH and voltage. TiO₂ has been extensively used in different photocatalytic applications, including water and air-purification, water splitting, self-cleaning materials, and for the degradation of cancer cells and viruses.[1−4] However, the band gap of TiO₂ (anatase phase ≈ 3.2 eV) lies in the UV region of the electromagnetic spectrum, which minimizes its maximum solar efficiency. This has led to a large research drive to develop doping strategies in an effort to decrease the band gap of TiO₂.

Nonmetal acceptor doping has been extensively employed to extend the absorption properties of TiO₂ into the visible range. This type of doping should simultaneously raise the valence band maximum of TiO₂ (causing a redshift of the absorption edge) and reduce the number of recombination centers,[5] with nitrogen being the most commonly studied dopant. Despite the

wealth of literature on N-doped TiO₂,[6] there is little consensus on whether this leads to an overall improvement in sunlight driven photocatalysis.[7−12]

Cationic dopants with a higher oxidation state than Ti^{4+} do not reduce the visible light response of anatase TiO₂. Instead they act as electron donors, injecting electrons into the conduction band, and can transform anatase into a transparent conducting oxide (TCO). This transformation normally occurs with a blue shift of the optical absorption and a dramatic reduction in resistivity, with typical donor dopants being Nb, Ta, and W.[13−15] The use of TiO₂-based materials for TCO applications presents advantages compared to indium-based TCO materials, such as high refractive index, high transmittance in the infrared region, and high chemical stability as

well as a significant reduction in the production cost.[16] Ta and Nb doping show electrical and optical properties comparable to ITO materials; however, W and F doping do not yield low enough resistivities, which could be attributed to a charge carrier concentration effect (i.e., lower donation efficiency).[17] In all cases, however, a penalty in terms of reduced photocatalytic performance must often be paid.

The choice of phosphorus as a dopant allows the possibility of both cationic (P^{5+}) and anionic (P^{3-}) doping of anatase TiO$_2$. In the pentavalent state (P^{5+}), phosphorus can induce a blue-shift and an increase in the free charge carriers of phosphorus-doped TiO$_2$ films. In addition, P is a much cheaper and more earth abundant dopant than either Nb or Ta and so represents an attractive alternative with a view to large scale industrial deployment. Therefore, the synthesis of phosphorus-doped films could present a new approach to produce TCO materials. To the best of our knowledge, the electrical properties of phosphorus-doped TiO$_2$ films are yet to be studied.

Phosphorus-doped TiO$_2$ films (henceforth, P-TiO$_2$) have been previously synthesized via the sol−gel method. These P-doped materials were reported to possess a single oxidation state assigned to a phosphate state (P^{5+}).[18−21] Different methods such as degradation of dyes (methyl orange (MO) and methylene blue (MB)) and organic compounds (n-pentane and ethanol) were performed to assess the photocatalytic activity of the samples. These tests showed different photocatalytic values, which could be attributed to varying phosphate content and surface area of the samples.

In the present work, APCVD was used to produce high quality P-TiO$_2$ films.[22] This method presents advantages over the sol−gel route, as the material is grown directly at high temperature. This avoids the amorphous to crystalline transition imposed in sol−gel that could drastically alter the nature and content of the dopant.[18−20] Interestingly, our CVD route can achieve multivalent P-doping, where cationic P^{5+} and anionic P^{3-} are present.[7] This paper explores the nature and effect of P-doping TiO$_2$ thin films on the electronic and photocatalytic functionality.

2. EXPERIMENTAL SECTION

All chemicals were purchased from Sigma-Aldrich. Titanium tetrachloride (TiCl$_4$, 99.9%), ethyl acetate (C$_4$H$_8$O$_2$, 99.8%), and triethyl phosphate ((C$_2$H$_5$O)$_3$PO, 99.8%) were used as titanium, oxygen, and phosphorus sources, respectively. Octadecanoic (stearic) acid (CH$_3$(CH$_2$)$_{15}$CH$_2$CHO$_2$, 98.5%) was used to perform the photocatalytic test.

2.1. Atmospheric Pressure Chemical Vapor Deposition Apparatus. The whole CVD apparatus was kept at high temperature (473 K). The precursors were heated independently in stainless steel bubblers in order to generate enough vapor pressure to be carried into the reactor. Preheated nitrogen (473 K) was used as the carrier gas (supplied by BOC), to drag the precursor vapors into stainless steel mixing chambers kept at 523 K, under controlled flow rate conditions. A plain nitrogen flow pushed the gas mixture through a triple baffle manifold that produced wide laminar flow into the reactor. The reactor consisted of a graphite block (320 mm-long × 150 mm-width) contained within a quartz glass tube and was heated using three embedded Whatman heater cartridges. The temperature was controlled using Pt−Rh thermocouples.

Films were grown at 773 K on float glass substrates (89 × 225 × 4 mm) supplied by the Pilkington NSG Group, which are precoated with a SiO$_2$ barrier layer to prevent ion diffusion from the glass into the film. The glass substrates were thoroughly cleaned using acetone

(99%), isopropanol (99.9%), and distilled water and dried in air prior to use.

2.2. Analytical Methods. X-ray diffraction (XRD) analysis was performed using a Bruker-Axs D8 (Lynxeye XE) diffractometer. The instrument operates with a Cu X-ray source, monochromated ($K\alpha_1$, 1.54 Å). Films were analyzed with a glancing incident angle (θ) of 1°. Le Bail fits were made to the diffraction patterns, using the anatase structure parameters from Joint Committee on Powder Diffraction Standards (JCPDS), through the GSAS and EXPGUI software suite. UV/vis spectroscopy was performed using a double monochromated PerkinElmer Lambda 950 UV/vis/NIR spectrophotometer in the 300−2500 nm range. Reflectance spectra were recorded for different positions in the range 300−2500 nm on a Helios double beam instrument standardized relative to a silicon mirror, which allowed the thickness of the films to be determined via Swanepoel method.[23] The latter measurements were confirmed for selected samples using side-view scanning electron microscopy (SEM). The SEM studies were carried out using JEOL 6301 (5 kV) and a JEOL JSM-6700F field emission instruments, and the Oxford software INCA was used by EDX. Atomic force microscopy (AFM) was conducted using a Bruker Icon system running in PeakForce Quantitative Nanomechanical Property Mapping (QNM) mode. Bruker NCHV (etched silicon) tips were used in contact mode over a selection of 5 μm × 5 μm areas to measure the topography of the samples. X-ray photoelectron spectroscopy (XPS) was performed using a Thermo K alpha spectrometer with monochromated Al Kα radiation, a dual beam charge compensation system, and constant pass energy of 50 eV. Survey scans were collected in the range 0−1200 eV. High-resolution peaks were used for the principal peaks of Ti (2p), O (1s), P (2p), C (1s), and Si (2p). The peaks were modeled using relative sensitivity factors to calculate the film composition. The area underneath these bands is an indication of the concentration of element within the region of analysis (spot size 400 μm).

2.3. Transient Absorption Spectroscopy. Charge carrier dynamics of TiO$_2$ films were measured using transient absorption spectroscopy (TAS) from the microsecond−second time scale at room temperature ($\approx$ 297 K). The TAS apparatus has been described in detail elsewhere.[24] In brief, a 75 W Xe lamp is used as a probe beam with a monochromator placed before the sample. The change in transmitted light is measured by a Si PIN photodiode after a UV laser excitation pulse is applied on the sample using the third harmonic of a Nd:YAG laser (355 nm, 6 ns pulse width). Reasonably low laser intensities were used ($\approx$500 μJ cm^{-2} pulse^{-1}) with a laser repetition rate of 1 Hz. Each TAS trace is the result of averaging between 50 and 500 scans.

2.4. Hall Effect. Hall Effect probe measurements were conducted at room temperature on an Ecopia HMS-3000 device in the Van der Pauw configuration. Measurements were acquired at 0.58 T with a variable current of 1−300 μA, on square cut samples with soldered indium−tin ohmic contacts, the integrity of which were tested prior to measurement.

2.5. Photocatalytic Test. The photocatalytic performance of the films synthesized in this work was evaluated during photodegradation of octadecanoic (stearic) acid (95%, Sigma-Aldrich). Films were dip-coated with a thin layer of stearic acid using a 0.05 M solution in chloroform. The photocatalytic activity of samples was measured under UVA (Vilber-Lourmat, 2 × 8 W, 365 nm, 1.2 mW cm^{-2}) illumination. A PerkinElmer RX-I Fourier transform infrared (FTIR) spectrometer was used to monitor the degradation of the overlain stearic acid.

The integrated areas between the characteristic C−H infrared bands at 2958, 2923, and 2853 cm^{-1} were calculated. The photoactivity rates were estimated from linear regression of the initial 30−40% of the degradation, where the reaction has been shown to possess zero-order reaction kinetics above a critical stearic acid concentration. Using a conversion factor, the number of molecules of stearic acid degraded was estimated considering that 1 cm^{-1} of integrated area corresponds to 9.7 × 10^{15} molecules of stearic acid.[25] Formal quantum efficiencies (FQE), defined as molecules of acid degraded per incident photon

Table 1. Experimental Details for the Deposition of Undoped and P-Doped TiO₂ Thin Films[a]

	experimental details				
sample	P bubbler T (K)	P mass flow (10^{-3}) (g min^{-1})	[P] total (atom %)	[P^{5+}] (atom %)	[P^{3-}] (atom %)
Anatase	--	--	--	--	--
P^{5+}/P^{3-} = 1:0(a)	365	0.13	0.50 ± 0.18	0.50 ± 0.18	--
P^{5+}/P^{3-} = 1:0(b)	364	0.24	0.90 ± 0.37	0.90 ± 0.37	--
P^{5+}/P^{3-} = 1:1	355	0.38	2.27 ± 0.58	1.17 ± 0.51	1.10 ± 0.65
P^{5+}/P^{3-} = 2:1	363	0.57	2.98 ± 0.62	2.04 ± 0.68	0.94 ± 0.37

[a]The temperature and mass flow conditions were constant for metal (TiCl₄) and oxygen (C₄H₈O₂) precursors: 341 and 311 K and 6.7×10^{-3} and 3.1×10^{-3} g min^{-1}, respectively.

(molecule photon^{-1}) were calculated assuming all incident photons had the same energy (3.4 eV) and were absorbed by the films.

3. RESULTS AND DISCUSSION

3.1. Films Synthesis. Phosphorus-doped TiO₂ thin films were grown on glass by APCVD, from the reaction of titanium tetrachloride (TiCl₄), ethyl acetate (EtOAc), and triethyl phosphate ((EtO)₃PO) at 773 K, following eq 1.

$$TiCl_4 + CH_3COOC_2H_5 + (C_2H_5O)_3PO$$
$$\rightarrow Ti_{1-x}O_{2-x}P_x + by\text{-}products \quad (1)$$
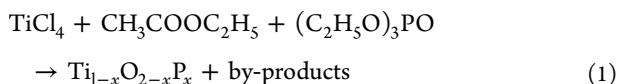
The particular reaction mechanism between TiCl₄ and EtOAc is not known. A possible mechanism involves the hydrolysis of TiCl₄ (eq 2)[26] via decomposition of ethyl acetate to form ketene and ethanol and subsequent dehydration of ethanol to form ethene and water.

$$CH_3COOC_2H_5 \rightarrow CH_3CH_2OH + C_2H_2O \quad (2a)$$

$$CH_3CH_2OH \rightarrow H_2O + C_2H_4 \quad (2b)$$

$$H_2O + TiCl_4 \rightarrow TiO_2 + 4HCl \quad (2c)$$
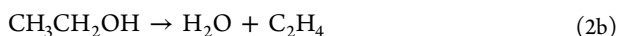
In phosphorus doping, the vapor pressure of the phosphorus source was controlled by heating the stainless steel bubbler to 363 K. Film thickness (as determined from side-on SEM and the optical Swanepoel method)[23] varied between 450 and 1050 nm depending on the precursor flow rate. This variation in the thickness across the substrate corresponds to the presence of optical interference, each color band corresponding to a different region of thickness.[27] The corresponding flow rates and phosphorus content are listed in Table 1. All films were adhesive, passing the Scotch tape test[28] (no particles were peeled off from the substrate), resisted scratching with a steel scalpel,[29] and are indefinitely stable in air over several months. The films showed no pinhole defects, and no particulates were observed in the exhaust gas.

X-ray photoelectron spectroscopy (XPS) was used to study the nature and concentration of the phosphorus dopant in TiO₂. As XPS is a surface-sensitive technique (≤10 nm),[30] several depths within the bulk were investigated by etching the surface with argon sputtering. Previous reports have shown that phosphorus can substitutionally enter the TiO₂ as either P^{5+} cations that replace Ti^{4+} lattice sites or P^{3-} anions that replace O^{2-} lattice sites, which are commonly assigned to XPS P 2p binding energies of ca. 135 and 129 eV, respectively.[18,31−33]

The P-doped TiO₂ films synthesized in this work showed a single surface peak at 133.7 eV, which was assigned to P^{5+} cations (Figure 1).[18,20] Interestingly, surface etching revealed an additional P 2p environment in the bulk of highly doped samples (≥2.3 atom %). This bulk peak at 128.8 eV was
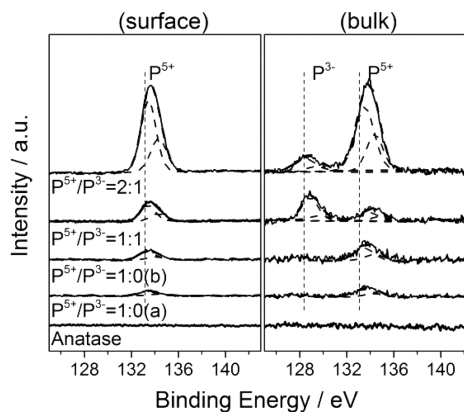
Figure 1. XPS spectra of surface (left) and bulk average (right) species in the P 2p environment (assignments included) of P-TiO₂ films (P^{5+}/P^{3-} = 1:0(a), P^{5+}/P^{3-} = 1:0(b), P^{5+}/P^{3-} = 1:1, and P^{5+}/P^{3-} = 2:1) and as-deposited undoped TiO₂ film used as reference. The solid lines represent experimental data and dotted lines represent the deconvolution of each chemical state into its respective 2p$_{3/2}$ and 2p$_{1/2}$ environments.

assigned to P^{3-} anions (Figure 1).[33,34] It is known that the etching procedure can change the oxidation state of elements during XPS depth profiling;[35] however, this is unlikely in the hypothetical case of a reduction from P^{5+} to P^{3-}, since argon sputtering typically encourages oxidation. The fact that solely P^{5+} was present at the surface, even in samples that contained both P^{5+} and P^{3-} in the bulk, was attributed to surface oxidation on exposure to air.

The relevant samples in this work were given a nomenclature based on the approximate relative ratio of P^{5+}/P^{3-}, as determined by XPS analysis of the P 2p environment. Four distinct P-TiO₂ samples were studied herein (Table 1): P^{5+}/P^{3-} = 1:0(a), P^{5+}/P^{3-} = 1:0(b), P^{5+}/P^{3-} = 1:1, and P^{5+}/P^{3-} = 2:1. The content of phosphorus in these samples was 0.50, 0.90, 2.27, and 2.98 atom %, respectively (Table 1).

3.2. Structural Properties. X-ray diffraction analysis showed that all undoped and P-doped TiO₂ thin films comprised purely the anatase phase structure. No traces of the rutile phase or any additional phosphorus-based structures were observed (see Supporting Information Figure 1S). The diffraction peaks shifted substantially in P-doped samples relative to undoped samples. Patterns were fit to a Le Bail refined model in order to quantify these changes in the lattice. The largest changes were found in the tetragonal c axis. The film that contained the lowest level of P doping (P^{5+}/P^{3-} = 1:0(a)) showed the most contracted unit cell (135.7 ± 0.08 Å³) relative to pure anatase (136.74 ± 0.08 Å³). Samples with low levels of P-doping, P^{5+}/P^{3-} = 1:0(a) (0.50 atom %) and P^{5+}/P^{3-} = 1:0(b) (0.90 atom %), showed only one P 2p

Table 2. Physical and Functional Characterization Data for Undoped and P-Doped TiO$_2$ Films Acquired via X-ray Diffraction Analysis (XRD), Raman Spectroscopy, UV/Visible Absorption Spectroscopy, X-ray Photoelectron Spectroscopy (XPS), Transient Absorption Spectroscopy (TAS), Atomic Force Microscopy (AFM), Photocatalytic Degradation of Stearic Acid (SA), and Van der Pauw and Hall Effect Electrical Measurements

	physical Properties							
	X-ray diffraction			spectroscopy				TAS
sample	a [Å]	c [Å]	vol [Å^3]	raman (E_g) cm^{-1}	band gap (eV)	d [nm min^{-1}]^a	T % @ 2500 nm^b	$t_{1/2}$ from 2 μs
anatase	3.787(1)	9.533(6)	136.74(6)	143.9	3.22	305	73.2	58
P^{5+}/P^{3-} = 1:0(a)	3.782(1)	9.505(6)	135.67(4)	141.7	3.36	315	66.8	--
P^{5+}/P^{3-} = 1:0(b)	3.780(1)	9.492(5)	135.93(8)	141.4	3.39	350	67.3	14
P^{5+}/P^{3-} = 1:1	3.785(2)	9.520(6)	136.39(6)	143.2	3.28	385	72.3	3.1
P^{5+}/P^{3-} = 2:1	3.788(1)	9.512(2)	136.53(3)	142.7	3.24	450	74.8	19

	functional properties			electrical properties		
	AFM	photocatalysis		Hall effect probe		
sample	surface area (μm^2)	FQE (10^{-4})	FQY (10^{-4})	ρ (Ω cm)	μ (cm^2 V^{-1} s^{-1})	n (10^{19} cm^{-3})
anatase	29.35 ± 0.39	0.86 ± 0.01	1.34 ± 0.02	--	--	--
P^{5+}/P^{3-} = 1:0(a)	--	0.33 ± 0.01	0.65 ± 0.02	1.69 ± 0.42	0.81 ± 0.13	0.49 ± 0.21
P^{5+}/P^{3-} = 1:0(b)	29.00 ± 0.18	0.47 ± 0.02	0.78 ± 0.03	--	--	--
P^{5+}/P^{3-} = 1:1	--	0.01 ± 0.01	0.01 ± 0.01	8.18 ± 2.13	0.10 ± 0.04	2.21 ± 1.76
P^{5+}/P^{3-} = 2:1	30.13 ± 0.57	0.55 ± 0.02	0.82 ± 0.02	6.49 ± 1.89	0.09 ± 0.05	1.54 ± 1.11

$^a d$ = film thickness. ^{b}Average between 0 and 2500 nm. Numbers in parentheses represent the error on the last digit.

environment, attributed to P^{5+} states,[21,26] and these P^{5+} cations are most likely substituted on Ti^{4+} sites. The large contractions in the unit cell were explained in terms of the differences in ionic radii, where 6 coordinate complexes of P^{5+} and Ti^{4+} show average ionic radii of 0.380 and 0.605 Å, respectively. In contrast, films with higher levels of P-doping, P^{5+}/P^{3-} = 1:1 (2.27 atom %) and P^{5+}/P^{3-} = 2:1 (2.98 atom %), showed two different P 2p environments, attributed to P^{5+} and P^{3-} states,[18,31−33] where these P^{3-} anions most likely substituted O^{2-} sites. The contractions in the unit cell were suppressed when both types of P-dopant were present.

This was because the P^{3-} states (2.10 Å) that replaced the O^{2-} sites (1.40 Å) were larger and thus offset the contractions caused by P^{5+} insertion. An additional effect was observed where the preferential growth in particular diffraction planes changed with P-doping level. In a single crystal, growth in the (101) diffraction plane of TiO$_2$ is most prominent. However, films grown by APCVD tend to show the most substantial increase in preferred growth in the (211) diffraction plane alongside a suppressed growth in the (101) plane. Nevertheless, Hyett et al.[36] found that the photocatalytic activities of TiO$_2$ films grown by APCVD did not change much with changes in preferred growth. In undoped and P-doped films of low level doping, films showed the most preferred growth in the (211) diffraction plane. At higher levels of P-doping, preferred growth was most prominent in the (101) diffraction plane (see Supporting Information Figure 1S). A similar trend was also observed by Kafizas et al.[17] and Bhachu et al.[14] in Nb-doped TiO$_2$ films grown by APCVD, where the most preferred growth changed from the (101) to the (211) planes at high concentrations of Nb.

Further structural studies were carried out using Raman spectroscopy. The Raman studies confirmed the results observed through X-ray diffraction analysis, as solely anatase phase of TiO$_2$ was present in all films. The major scattering E_g band, typically found at 144 cm^{-1} in undoped anatase, shifted to lower wavenumbers upon P doping (Table 2). The E_g mode represents phonons operating primarily in the a-axis of the tetragonal unit cell.[37] A clear trend is observed between the

degree of red-shift in the E_g band and contraction in unit cell volume (Table 2), where the most red-shifted bands were found in the most contracted unit cells (i.e., samples P^{5+}/P^{3-} = 1:0(a) and P^{5+}/P^{3-} = 1:0(b)) (see Supporting Information Figures 2S and 3S).

3.3. Film Morphology. Scanning electron microscopy (SEM) analysis was used to investigate the structural morphologies of both undoped and P-doped TiO$_2$ samples. Undoped TiO$_2$ films showed well-defined shell-shaped aggregated particles (Figure 2a). However, the incorporation
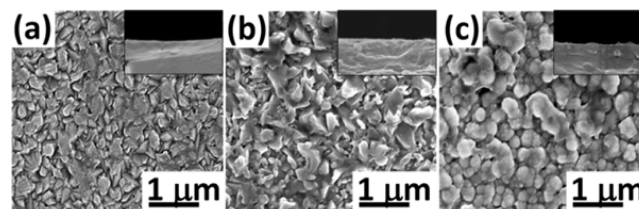
Figure 2. Scanning electron microscopy (SEM) images of typical (a) undoped TiO$_2$ and (b) low concentration and (c) high concentration P-TiO$_2$ films. The inset shows side-view SEM of the films.

of phosphorus in the structure of the films caused a drastic change in the structural morphology. At low levels of P-doping (sample P^{5+}/P^{3-} = 1:0(b)), larger particles, more jagged in shape, were observed (Figure 2b). At high levels of P-doping (P^{5+}/P^{3-} = 2:1), even larger and more rounded bulb-shaped particles were observed (Figure 2c). Overall, P-doping increased particle size.

Further inspection using atomic force microscopy (AFM) was performed six times locally for each sample. Scan areas of 5 μm × 5 μm were sampled with a 20 nm special frequency using a contact (PeakForce) scanning mode. The roughness induced surface area increase was calculated by averaging the projected surface areas for each of the samples. In line with SEM studies, progressively larger and more rounded particles were observed upon P-doping (Figure 3). The root mean squared roughness increased significantly from 16 nm for undoped TiO$_2$ to 51 nm
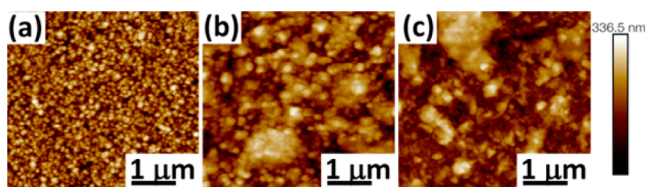
Figure 3. Atomic force microscopy (AFM) images of typical (a) undoped TiO_2 and P-doped TiO_2 films, with (b) low levels of phosphorus (P^{5+}/P^{3-} = 1:0 (0.90 atom %)) and (c) high levels of phosphorus (P^{5+}/P^{3-} = 2:1 (2.98 atom %)).

for high levels of P doping; however, the projected surface area saw only a slight increase (from 29.4 μm^2 to 30.1 μm^2) as the peaks became more sparse.

However, the calculated surface areas ranged from just 29.35 ± 0.39 μm^2 in undoped TiO_2 films to 29.00 ± 0.18 μm^2 and 30.13 ± 0.63 μm^2 in P^{5+}/P^{3-} =1:0(b) and P^{5+}/P^{3-} =2:1 samples, respectively (Table 2).

3.4. Optical Properties. The undoped TiO_2 thin films produced in this work were highly transparent. The incorporation of low P concentrations (<1 atom %) resulted in films with a blue/yellow tinge, evidenced by a slight dip in transmission in the green-red absorption region from ≈600 to 2000 nm (Figure 4). Indeed, Tauc plot analysis (Figure 4,
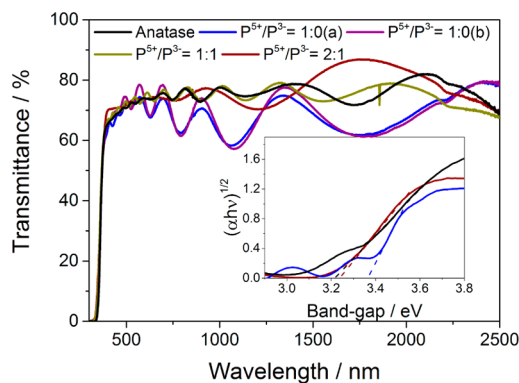
Figure 4. UV−vis spectra of selected P-TiO_2 films (P^{5+}/P^{3-} = 1:0(a), P^{5+}/P^{3-} = 1:0(b), P^{5+}/P^{3-} = 1:1, and P^{5+}/P^{3-} = 2:1). Undoped TiO_2 (black solid line) is included for reference. The inset shows band gap measurements derived from Tauc plot analysis for P-doped films with low P levels, P^{5+}/P^{3-} = 1:0(a) (burgundy line), and high P levels, P^{5+}/P^{3-} = 2:1 (blue line). The black line in the inset corresponds to undoped TiO_2.

inset) showed a slight shift in absorption into the blue region for these P-TiO_2 samples, with band gap energies estimated around 3.4 eV compared to undoped films (∼3.2 eV). Surprisingly, doped films with high P content (>1 atom %) did not show this blue shift, and the corresponding band gap energies were comparable to undoped TiO_2. The change in band gap energy was discussed in terms of the different properties of the two oxidation states of phosphorus (P^{5+} and P^{3-}) in the TiO_2 structure. The increase in band gap energy was only observed for films containing low concentrations of phosphorus and only P^{5+} cations. This increase would certainly not be expected from the incorporation of P^{3-} anions into O^{2-} lattice sites. The density of states of TiO_2 is primarily composed of O 2p orbitals in the valence band and Ti 3d orbitals in the conduction band. Anionic dopants, such as P^{3-}, typically replace O^{2-} sites and thus alter primarily the valence band of

TiO_2. This is the case of N^{3-} dopants, for instance, which occupy O^{2-} sites, and then mixing of N 2p and O 2p orbitals pushes the valence band upward, thus causing a *decrease* in band gap energy (i.e., red-shift of absorption spectrum).[6,38,39] One might attribute this to a Moss-Burstein shift that occurs when the carrier concentration is high enough to cause degeneracy and raise the conduction band minimum by occupancy. However, as discussed below, Hall Effect probe measurements showed that the charge carrier concentrations were very low when merely P^{5+} was present ($n ≈ 5 × 10^{18}$ cm^{-3}) compared to those recorded at high P levels ($1 × 10^{19} ≤ n ≤ 5 × 10^{19}$ cm^{-3}), where both P^{5+} and P^{3-} were presented. If a Moss-Burstein shift was the reason for a blue-shift in band gap energy, then the same phenomenon should also have been observed in the case of the latter samples. Another possibility is that these differences in band gap were due to changes in unit cell volume. As inferred from our XRD analysis, little or no disruption of the lattice was found in samples containing both P^{5+} and P^{3-}, while samples containing P^{5+} species only resulted in unit cell expansion, greater average distance between the ions within the lattice, and thus widened density of states. The intrinsic disorder caused by having a significant proportion of both P^{5+} and P^{3-} anions in the structure could also have an impact on the measure band gaps. At present the exact origin of these band gap trends remains unanswered.

Transient absorption spectroscopy (TAS) measurements on the microsecond to second time scale were used to investigate the lifetime and population of photogenerated charge carriers in both undoped and P-doped samples (Figure 5). Transient
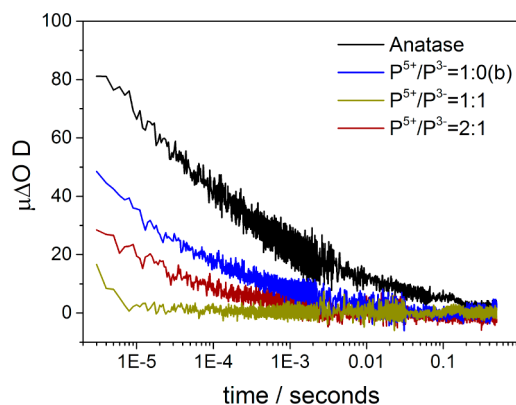
Figure 5. Transient absorption kinetic decays on the microsecond to second time-scale, normalized at 2 μs, was used to investigate the lifetimes of photogenerated charge carriers for undoped (black line) and P-doped TiO_2 films (P^{5+}/P^{3-} = 1:0(b), blue line; P^{5+}/P^{3-} = 1:1, green line; and P^{5+}/P^{3-} = 2:1, burgundy line).

absorption spectroscopy (TAS) is a form of laser flash spectroscopy that tracks transient changes in absorption after an excitation pulse. In many semiconductor photocatalysts, these transient changes in absorption have been shown to be directly related to transient changes in photogenerated charge.[40−42] It has been shown that the population and dynamics of photogenerated electrons or holes could be studied in TiO_2 by tracking transient absorbance changes at particular wavelengths.[43] Measurements were conducted in argon (an inert environment), which meant the photogenerated charges could only recombine (i.e., no photocatalytic processes could occur). As the photogenerated charges recombined, the change in transient absorption decreased toward zero net change (i.e.,

complete recombination of charge). The speed at which recombination occurs dictates the natural lifetime of photo-generated charge in a given material. In undoped anatase TiO_2, photogenerated charges naturally recombine within 100 ms and show a power law decay typical of the trap/detrapping movement of charge.[24] Each TAS spectrum was measured from the microsecond to second time scale, which misses the stage of initial charge generation and trapping (femtosecond to picosecond time scale) but covers the time scale where most photocatalytic processes typically occur such as the reduction of O_2,[44] the oxidation of NO,[45] and the oxidation of water.[46]

A 355 nm laser pulse was used to excite our samples, creating photogenerated charges in the semiconductor alongside a transient change in absorption (Figure 5). Our series of samples had similar levels of absorption at 355 nm (Figure 4), which allowed us to also compare changes in population. At 2 μs, the undoped TiO_2 sample possessed the highest absorbance. This meant that more photogenerated charges were present in this material at this time-scale compared with the P-doped samples, even though all samples would have absorbed a similar level of light from the laser pulse. Moreover, when we compared the time it took for the initial absorption signal at 2 μs to decrease to half of its initial value ($t_{1/2}$) it was observed that recombination was slowest in the undoped sample (Table 2). Undoped anatase TiO_2 possessed the longest lifetime with a $t_{1/2}$ of 58 μs. The next longest lived charges were found in samples P^{5+}/P^{3-} = 2:1 and P^{5+}/P^{3-} = 1:0(b), with a $t_{1/2}$ of 19 and 14 μs, respectively. The shortest lived photogenerated charge was found in sample P^{5+}/P^{3-} = 1:1, with a $t_{1/2}$ of 3.1 μs.

Overall, a general trend was observed where P-doping decreased the lifetime of photogenerated charge in TiO_2. It is often argued that doping TiO_2 typically encourages recombination, where the dopant sites act as centers for recombination.[47] Interestingly, the rate of recombination varied substantially in our P-doped TiO_2 materials. No complete correlation between recombination rate and P-doping levels could be established; however, our findings do suggest that a faster recombination rate occurs when the P^{5+} and P^{3-} concentration are equivalent.

3.5. Functional Properties. *Electrical Properties: Hall Effect Probe.* Electrical properties of P-doped TiO_2 films were investigated by room temperature Hall Effect probe measurements in the van der Pauw configuration on samples made with soldered indium−tin contacts. Several areas in each of the low, mid, and high dopant levels in P-TiO_2 were examined and area-specific XPS data obtained. Figure 6 shows median values and standard error for carrier mobility, carrier density, and resistivity of the P-TiO_2 films as a function of overall P-dopant and relative presence of P^{3-}. All P-TiO_2 films display n-type conductivity, with different electrical conductivity effects depending on the oxidation state of the dopant (P^{5+} and P^{3-}). Furthermore, the dopant seems to induce different electrical conductivity effects depending on oxidation state; the presence of the P^{3-} state (substituting the O^{2-} lattice site and neutralizing an electron in the system) corresponds to a decrease in both resistivity and charge carrier density while the P^{5+} state (substituting on the Ti^{4+} site and liberating an electron) effects an increase in electrical conductivity. Only at low phosphorus doping levels is the P^{5+} state present alone (<1 atom %), whereas at higher doping levels (from ≈2 atom %) the P^{3-} state is also detectable.

The dramatic increase in charge carrier density values indicates that effective P-doping induces a crossover into
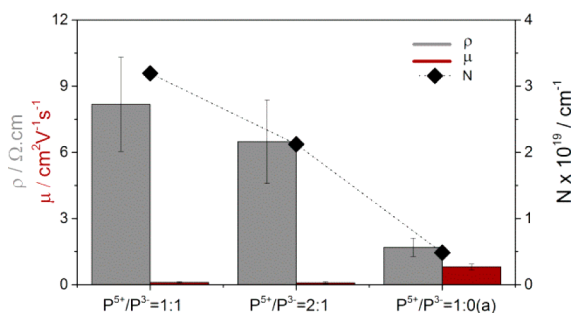
Figure 6. Comparison of Hall Effect probe measured resistivity (gray bars), charge carrier mobility (burgundy bars), and carrier density (full diamonds) for P-doped TiO_2 thin films; P^{5+}/P^{3-} = 1:1, P^{5+}/P^{3-} = 2:1, and P^{5+}/P^{3-} = 1:0(a). Standard errors are included for median electrical property values.

semiconductor degeneracy, achieving a more "metallic" character in accordance with the Mott metal-to-insulator transition. Such carrier concentration levels are not achievable in nominally undoped TiO_2 films that allow conduction through oxygen vacancies. The carriers are thought to transfer via a band process. Carrier density shows a typical transition from high resistivity, to low resistivity at an idealized dopant level (≈ 1 atom %), followed again by an increase in resistivity. This can be rationalized by considering the role of P dopants in TiO_2. At low doping levels P will enter the lattice in the Ti site, with an oxidation state of 5+. The ionic radius of six coordinated P^{5+} at 0.380 Å is smaller than that of Ti^{4+} (0.605 Å), so it will readily fit in that Ti lattice position. P^{3-}, however, is much larger than O^{2-}, and so will not be incorporated as readily into TiO_2. As the concentration of dopant is increased, the formation energy of the cationic dopant, which acts as a shallow donor and is in the P_{Ti}^{+1} charge state (Figure 7),
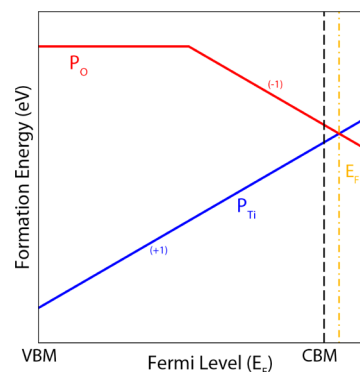
Figure 7. Schematic showing the mechanism of dopant self-compensation as the P-doping level is increased. The *y*-axis displays the formation energy of the defect species, and the *x*-axis shows the position of the Fermi level relative to the VBM and CBM for anatase TiO_2. For high doping levels (above the CBM), the Fermi level gets trapped (orange dot-dash vertical line) by the formation of P_O^{-1}.

increases over the range of the band gap. P on an oxygen site, however, acts as a p-type dopant, with the hole state localized on the p-states of the P dopants. At high Fermi levels, however, P_O^{-1} will start to become favorable. Once the concentrations of P dopant exceed ~1%, the P_O^{-1} starts to dominate, acting as a hole killer, and pinning the Fermi level above just the conduction band minimum (CBM). Any further increase of

the P doping concentration will just result in the decrease of the number of electrons in the system.

While the effective carrier density values are fairly impressive; $0.5-2.2 \times 10^{19}$ cm^{-3} (especially as compared to other nonmetal dopants such as fluorine), the carrier mobilities were low ($\approx$ 0.1−0.8 cm^2 V^{-1} s^{-1}) and attributed to ionized impurity scattering. Overall, the current effective resistivities (of the order of 10^0 Ω·cm) were too high for conventional TCO applications.

The marked decrease in mobility with phosphorus doping demonstrates the heavy ionized impurity scattering effect (whether direct or indirect) of the dopant. However, the presence of the P^{3-} state correlates with a larger decrease in carrier mobility. Indeed, whether the decrease in mobility is a result of the higher presence of the phosphorus dopant (which leads to the presence of P^{3-} above a threshold value) or to the anionic state itself is difficult to distinguish. However, our findings suggest that at similar levels of total P-doping, a greater relative presence of the P^{3-} state vs the P^{5+} state will result in a more severe decrease in mobility.

Photocatalytic Activity. The experimental observations reported on the photocatalytic activity of P-TiO$_2$ materials are very different. Typical synthesis methods, such as sol−gel, may produce materials with varying phosphate content and surface area, potentially affecting the performance of P-TiO$_2$ photocatalysts.[18−21] In contrast, APCVD allowed the synthesis of films with homogeneous P content across the bulk and also comparable surface properties. The synthesized films also allowed a thorough study of the correlation of P species and the photocatalytic properties of these materials. The photocatalytic activity of the P-TiO$_2$ films was evaluated during the degradation of stearic acid under UVA irradiation (1.2 mW cm^{-2}).[25] The overall photocatalytic reaction is given by eq 3.

$$CH_3(CH_2)_{16}CO_2 + 26O_2 \rightarrow 18CO_2 + 18H_2O \quad (3)$$
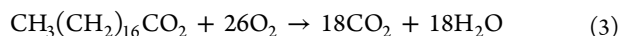
The photocatalytic process was monitored using FTIR, following the disappearance of characteristic C−H modes of the acid (2958, 2923, and 2853 cm^{-1}). The photocatalytic rates were estimated from linear regression of the initial steps (30−40%) of the curve of integrated area vs illumination time. The corresponding rates were expressed as formal quantum efficiencies (FQE), defined as molecules of stearic acid degraded over incident photons (units, molecule·photon^{-1}) (Figure 8). The variation in FQE values was discarded to be
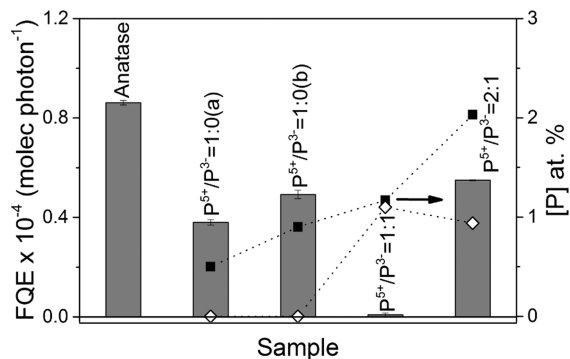
due to differences in physical properties of the films, since all films investigated showed comparable thicknesses and crystallinity, based on XRD and Raman analysis (see Supporting Information), as well as similar surface topography (Figures 2 and 3, Table 2). With the exception of sample P^{5+}/P^{3-} = 1:1, which showed no activity, most P-TiO$_2$ films showed moderate activities compared to undoped TiO$_2$ samples. This is surprising for highly conductive samples, since electrical conductivity is usually observed to the detriment of photocatalytic activity.[13] It is also worth noting that previous groups have observed far greater detriment when doping with nitrogen or sulfur.[36,48]

The film photocatalytic activities (Figure 8) could be correlated directly with photogenerated charge carrier lifetimes (Figure 5), where high lifetime resulted in high photocatalytic activity, undoped TiO$_2$ being the most active sample (FQE = 0.86 molecule·photon^{-1}; $t_{1/2}$ = 58 μs), followed by P^{5+}/P^{3-} = 2:1, P^{5+}/P^{3-} = 1:0(b), and P^{5+}/P^{3-} = 1:0(a) doped films (FQE = 0.55, 0.47, and 0.33 molecule·photon^{-1}; $t_{1/2}$ = 19, 14, and n/a μs, respectively). Sample P^{5+}/P^{3-} = 1:1 showed the lowest lifetime ($t_{1/2}$ = 3.1 μs) and no photocatalytic activity. These observations were attributed to the kinetics of the typical processes associated with photocatalysis on TiO$_2$. It is generally accepted that photocatalysis on TiO$_2$ proceeds through two avenues: (i) the reaction of holes with surface H$_2$O forming highly reactive hydroxyl radicals that subsequently degrade nearby organics or (ii) the reaction of electrons with O$_2$ forming highly reactive superoxide species that can also degrade nearby organics.[1] These two processes occur on different time-scales, where it has been shown that (i) holes can react with H$_2$O within 2 μs and (ii) electrons react with O$_2$ from 10−900 μs.[49] Our TAS studies showed that the sample with longest-lived photogenerated charge was undoped TiO$_2$. However, from just 2−58 μs, half of those charges had recombined. Given the slow reaction of electrons with O$_2$, we attribute the low efficiency in the photocatalytic degradation of stearic acid ($\approx$ 1.4%) to the predominance of recombination vs O$_2$ reduction.

Interestingly, samples with a predominant presence of P^{5+} showed high photocatalytic activity and electrical conductivity, while an equivalent presence of P^{3-} and P^{5+} resulted in inactive samples with negligible conductivity. The latter observation was attributed to the promotion of electron−hole recombination in P^{3-} sites (see Supporting Information Figure 5S), where the photogenerated charge rate in the most P^{3-}-rich sample (P^{5+}/P^{3-} = 1:1) decayed almost 20 times faster than that observed for undoped TiO$_2$ films (Figure 5).

4. CONCLUSIONS

A new strategy to synthesize P-doped TiO$_2$ films (either P^{5+} doped or P^{5+} and P^{3-} doped) using atmospheric pressure chemical vapor deposition (APCVD) has been presented. This is, to the best of our knowledge, the first example of APCVD synthesis to incorporate anionic phosphorus (P^{3-}) in TiO$_2$.

Transient absorption spectroscopy (TAS) showed an overall decrease of photogenerated charge carrier lifetimes upon the incorporation of phosphorus in TiO$_2$, particularly in the case of P^{3-} species. The impact of P groups was also consistent with a decrease in photocatalytic activity, evaluated during the mineralization of stearic acid. It was concluded that P^{3-} species contributed to a fast recombination of photogenerated charges, which was as high as 20 times faster in the most P^{3-}-rich sample

Figure 8. Formal quantum efficiencies obtained during photodegradation of stearic acid under UVA irradiation of selected P-TiO$_2$ films and undoped TiO$_2$ film, used as reference. The relative levels (%) of cation phosphorus (P^{5+}, full squares) and anion phosphorus (P^{3-}, empty diamonds) are indicated for comparison.

compared to the typical rates observed in undoped TiO₂ films and almost 6 times faster than corresponding P^{5+}-rich samples.

In addition, Hall Effect probe measurements showed that electrical conductivity was highest in samples rich in P^{5+} species as well. This is a significant result, since electrical conductivity often arises to the detriment of photocatalytic activity, and it means a step forward in the formation of novel multifunctional materials, with an optimal balance between self-cleaning and TCO properties—the frontier application of photocatalytic transparent conductors.

■ ASSOCIATED CONTENT

Ⓢ Supporting Information

Physical properties of the as-deposited films, X-ray Diffraction (Figure 1S), and Raman analysis (Figure 2S). Photocatalytic degradation of stearic acid under UVA light, infrared spectra, and integrated areas are shown in Figure 4S. A comparison between TAS analysis and degradation of stearic acid is shown in Figure 5S. The Supporting Information is available free of charge on the ACS Publications website at DOI: 10.1021/cm504734a.

■ AUTHOR INFORMATION

Corresponding Author
*(I.P. Parkin) E-mail: i.p.parkin@ucl.ac.uk. Tel.: +44 020 7679 4669. Fax: +44 020 7679 7463.

Notes
The authors declare no competing financial interest.

■ ACKNOWLEDGMENTS

■ ABBREVIATIONS

APCVD, atmospheric pressure chemical vapor deposition; TCO, transparent conducting oxides; XRD, X-ray diffraction; SEM, scanning electron microscopy; AFM, atomic force microscopy; XPS, X-ray photoelectron spectroscopy; TAS, transient absorption spectroscopy

■ REFERENCES

(1) Mills, A.; Le Hunte, S. *J. Photochem. Photobiol., A* **1997**, *108*, 1.
(2) Dunnill, C. W. H.; Aiken, Z. A.; Pratten, J.; Wilson, M.; Morgan, D. J.; Parkin, I. P. *J. Photochem. Photobiol., A* **2009**, *207*, 244.
(3) Page, K.; Palgrave, R. G.; Parkin, I. P.; Wilson, M.; Savin, S. L. P.; Chadwick, A. V. *J. Mater. Chem.* **2007**, *17*, 95.
(4) Kafizas, A.; Kellici, S.; Darr, J. A.; Parkin, I. P. *J. Photochem. Photobiol., A* **2009**, *204*, 183.
(5) Korosi, L.; Oszko, A.; Galbacs, G.; Richardt, A.; Zollmer, V.; Dekany, I. *Appl. Catal., B* **2007**, *77*, 175.
(6) Asahi, R.; Morikawa, T.; Ohwaki, T.; Aoki, K.; Taga, Y. *Science* **2001**, *293*, 269.
(7) Emeline, A.; Kuznetsov, V. N.; Rybchuk, V. K.; Serpone, N. *Int. J. Photoenergy* **2008**, *2008*, 1.
(8) Zaleska, A. *Recent Pat. Eng.* **2008**, *2*, 157.
(9) Viswanathan, B.; Krishanmurthy, K. R. *Int. J. Photoenergy* **2012**, *2012*, 1.
(10) Zhang, J.; Wu, Y.; Xing, M.; Leghari, S. A. K.; Sajjad, S. *Energy Environ. Sci.* **2010**, *3*, 715.
(11) Asahi, R.; Morikawa, T. *Chem. Phys.* **2007**, *339*, 57.
(12) Asahi, R.; Morikawa, T.; Hazama, H.; Matsubara, M. *J. Phys.: Condens. Matter* **2008**, *20*, 064227.
(13) Kafizas, A.; Noor, N.; Carmichael, P.; Scanlon, D. O.; Carmalt, C. J.; Parkin, I. P. *Adv. Funct. Mater.* **2013**, *24*, 1758.
(14) Bhachu, D.; Sathasivam, S.; Sankar, G.; Scanlon, D. O.; Cibin, G.; Carmalt, C. J.; Parkin, I. P.; Watson, G. W.; Bawaked, S. M.; Obaid, A. Y.; Al-Thabaiti, S.; Basahel, S. N. *Adv. Funct. Mater.* **2014**, *24*, 5075.
(15) Gillispie, M. A.; van Hest, M. F. A. M.; Dabney, M. S.; Perkins, J. D.; Ginley, D. S. *J. Mater. Res.* **2007**, *22*, 2832.
(16) Hitosugi, T.; Yamada, N.; Nakao, S.; Hirose, Y.; Hasegawa, T. *Phys. Status Solidi A* **2010**, *7*, 1529.
(17) Kafizas, A.; Noor, N.; Carmalt, C. J.; Parkin, I. P. *J. Mater. Chem. C* **2013**, *1*, 6335.
(18) Yu, J. C.; Zhang, L.; Zheng, Z.; Zhao, J. *Chem. Mater.* **2003**, *15*, 2280.
(19) Li, F.; Jiang, Y.; Xia, M.; Sun, M.; Xue, B.; Liu, D.; Zhang, X. *J. Mater. Chem. C* **2009**, *113*, 18134.
(20) Korosi, L.; Papp, S.; Bertoti, I.; Dekany, I. *Chem. Mater.* **2007**, *19*, 4811.
(21) Gopal, N. O.; Lo, H.; Ke, T.; Lee, C.; Chou, C.; Wu, J.; Sheu, S.; Ke, S. *J. Phys. Chem. C* **2012**, *116*, 16191.
(22) O'Neill, S. A.; Parkin, I. P.; Clark, R. J. H.; Mills, A.; Elliott, N. *J. Mater. Chem.* **2003**, *13*, 56.
(23) Swanepoel, R. *J. Phys. E: Instrum.* **1983**, *16*, 1214.
(24) Cowan, A. J.; Tang, J.; Leng, W.; Durrant, J. R.; Klug, D. R. *J. Phys. Chem. C* **2010**, *114*, 4208.
(25) Mills, A.; Wang, J. *J. Photochem. Photobiol., A* **2006**, *182*, 181.
(26) Evans, P.; Pemble, M. E.; Sheel, D. W. *Chem. Mater.* **2006**, *18*, 5750.
(27) Kafizas, A.; Parkin, I. P. *J. Am. Chem. Soc.* **2011**, *133*, 20458.
(28) Mittal, K. L. *Electrocomponent Sci. Technol.* **1976**, *3*, 21.
(29) Buttler, D. W.; Stoddart, C. T. H.; Stuart, P. R. *J. Phys. D: Appl. Phys.* **1970**, *3*, 877.
(30) Powell, C. J.; Jablonski, A.; Tilinin, I. S.; Tanuma, S.; Penn, D. R. *J. Electron Spectrosc. Relat. Phenom.* **1999**, *98–99*, 1.
(31) Splinter, S. J.; Rofagha, R.; McIntyre, N. S.; Erb, U. *Surf. Interface Anal.* **1996**, *24*, 181.
(32) Lin, L.; Lin, W.; Xie, J. L.; Zhu, Y. X.; Zhao, B. Y.; Xie, Y. C. *Appl. Catal., B* **2007**, *75*, 52.
(33) Blackman, C.; Carmalt, C. J.; Parkin, I. P.; O'Neill, S. *Chem. Mater.* **2002**, *14*, 3167.
(34) Myers, C. E.; Franzen, H. F.; Anderegg, J. W. *Inorg. Chem.* **1985**, *24*, 1822.
(35) Seah, M. P. *Surf. Interface Anal.* **1980**, *2*, 222.
(36) Hyett, G.; Green, M.; Parkin, I. P. *J. Am. Chem. Soc.* **2006**, *128*, 12147.
(37) Ohsaka, T.; Izumi, F.; Fujiki, Y. *J. Raman Spectrosc.* **1978**, *7*, 321.
(38) Yates, H. M.; Nolan, M. G.; Sheel, D. W.; Pemble, M. E. *J. Photochem. Photobiol., A* **2006**, *179*, 213.
(39) Finazzi, E.; Di Valentin, C.; Selloni, A.; Pacchioni, G. *J. Phys. Chem. C* **2007**, *111*, 9275.
(40) Pesci, F. M.; Cowan, A. J.; Alexander, B. D.; Durrant, J. R.; Klug, D. R. *J. Phys. Chem. Lett.* **2011**, *2*, 1900.
(41) Pendlebury, S. R.; Wang, X.; Le Formal, F.; Cornuz, M.; Kafizas, A.; Tilley, S. D.; Gratzel, M.; Durrant, J. R. *J. Am. Chem. Soc.* **2014**, *136*, 9854.
(42) Ma, Y.; Pendlebury, S. R.; Reynal, A.; Le Formal, F.; Durrant, J. R. *Chem. Sci.* **2014**, *5*, 2964.
(43) Fujishima, A.; Zhang, X.; Tryk, D. *Surf. Sci. Rep.* **2008**, *63*, 515.
(44) Peiro, A. M.; Colombo, C.; Doyle, G.; Nelson, J.; Mills, A.; Durrant, J. R. *J. Phys. Chem. B* **2006**, *110*, 23255.
(45) Devahasdin, S.; Fan, C.; Li, K.; Chen, D. H. *J. Photochem. Photobiol., A* **2003**, *156*, 161.
(46) Tang, J.; Durrant, J. R.; Klug, D. R. *J. Am. Chem. Soc.* **2008**, *130*, 13885.
(47) Kafizas, A.; Parkin, I. P. *J. Mater. Chem.* **2010**, *20*, 2157.
(48) Dunnill, C. W.; Aiken, Z. A.; Pratten, J.; Wilson, M.; Parkin, I. P. *Chem. Vap. Deposition* **2010**, *16*, 50.

(49) Yamakata, A.; Ishibashi, T.; Onishi, H. *J. Phys. Chem. B* **2001**, *105*, 7258.